RESEARCH ARTICLE
doi: 10.2306/scienceasia1513-1874.2026.048

ScienceAsia 52 (3): 2026: ID 2026048: **1–8**

Enhancing the performance of Cu_2O photocathode by tuning the band alignment for photoelectrochemical hydrogen production

Xue Luan[a,b,*], **Yongdan Li**[a,b], **Cuijuan Zhang**[a,b]

[a] Tianjin Key Laboratory of Applied Catalysis Science and Technology, State Key Laboratory of Chemical Engineering (Tianjin University), School of Chemical Engineering and Technology, Tianjin University, Tianjin 300072 China
[b] Collaborative Innovation Center of Chemical Science and Engineering (Tianjin), Tianjin 300072 China

*Corresponding author, e-mail: luan_233@163.com

Received 26 Aug 2025, Accepted 24 Apr 2026
Available online 29 May 2026

ABSTRACT: To alleviate the recombination of photo-generated charge carriers in the Cu_2O photocathode, heterojunction MO_x/Cu_2O (M = Zn, Ga, Al, Y) nanowire arrays were constructed by anodization and drop coating. The results show that the performance of heterojunction is strongly dependent on the band alignment. Y_2O_3/Cu_2O showed the smallest band offset and thus contributes to higher catalytic activity, with photocurrent density of −4.08 mA cm^{-2} at 0 V vs. reversible hydrogen electrode (RHE) under AM 1.5G illumination. Further studies reveal that the 600 °C-calcined Y_2O_3/Cu_2O showed the highest activity due to the synergistic effect of microstructure and electronic factors. In addition, the heterojunction could improve the stability, with 68.1% retention of photocurrent density compared with 20.4% for the bare one over 10 min-duration. This work demonstrates a facile strategy to tailor the photoelectrochemical performance of Cu_2O for hydrogen production.

KEYWORDS: photoelectrochemical water splitting, photocathode, cuprous oxide, heterojunction, band alignment

INTRODUCTION

Photoelectrochemical (PEC) water splitting is a promising method to produce hydrogen in a large scale utilizing the renewable but intermittent solar energy [1]. Since the pioneering work of Fujishima and Honda [2], many semiconductors have been proposed as effective catalysts for PEC water splitting, for example, TiO_2 [3], Fe_2O_3 [4], $BiVO_4$ [5] as photoanode to achieve oxygen evolution reaction. In contrast, limited attention has been paid to photocathode, where hydrogen evolution reaction (HER) takes place. Cuprous oxide (Cu_2O) is a well-known p-type semiconductor, characterized by its conduction band positioned at −0.7 V relative to the H^+/H_2 redox potential. This unique property makes Cu_2O highly suitable for facilitating the HER. It has a direct band gap of ∼2.0 eV and thus can absorb visible light, theoretically delivering a solar to hydrogen conversion efficiency of 18% and a theoretical photocurrent of −14.7 mA cm^{-2} for water splitting based on the AM 1.5G spectrum [6]. Moreover, Cu_2O is non-toxic and earth abundant, which can meet the global energy demand at a large scale. Accordingly, Cu_2O is considered as a very promising photocathode material.

Two of the main issues limiting Cu_2O as a photocathode for water splitting are the mismatch between the carrier diffusion length (20–100 nm) and the optical absorption depth (∼10 μm), and the poor stability in aqueous solution, which results in low activity and poor stability [7]. To mitigate those problems, Cu_2O nanowires and nanotubes with high aspect ratio are preferred, which possess long optical paths for efficient light absorption and short transport distances in the nm-scale radial direction. Better separation of charge carries can be achieved although accompanied with other problems [8–10]. Building p-n heterojunction is an effective approach to suppress the electron-hole recombination and protect Cu_2O from photo-corrosion simultaneously [11–25]. The Grätzel group prepared nanolayers of Al-doped ZnO (AZO) and TiO_2 on Cu_2O by atomic layer deposition (ALD), which delivered a photocurrent of −7.6 mA cm^{-2} at 0 V vs. reversible hydrogen electrode (RHE) with electrodeposited Pt nanoparticles and stable operation over 1 h due to the formation of staggered type-II band offset and conformal coating layers [11]. Later, they found that replacing AZO with Ga_2O_3 can further improve the photocurrent to −7.6 mA cm^{-2} and photocurrent onset to 1.0 V using NiMo as HER catalyst. Such enhancement is due to the small conduction band offset between Cu_2O and the coating layer (−0.26 eV for Ga_2O_3 vs. 1.08 eV for AZO), which effectively mitigates the recombination and further enhances the photovoltage [12]. Increased reports [13–19] show that selection of buffer layers with appropriate band offset can inhibit Cu_2O self-reduction as well as increase the photocurrent. Although many buffer layers such as ZnO [20, 21], TiO_2 [8, 11] and C_3N_4 [22, 23] have been proposed, Ga_2O_3 [12, 13, 24, 25] is most effective due to its similar electron affinity with Cu_2O. However, Ga_2O_3 is expensive and prepared usually by process-

complex and equipment-expensive ALD method, which probably pose serious limitation for its wide application.

Herein, we propose a new buffer layer, Y_2O_3, which is used to construct the Y_2O_3/Cu_2O heterojunction by simple and cost-effective anodization combined with drop coating. Such heterojunction shows higher photocurrent than Ga_2O_3/Cu_2O, delivering −4.08 mA cm^{-2} at 0 V vs. RHE under AM 1.5G illumination. The influence of preparation procedures on the catalytic performance is also discussed. The approach uses a simple solution as a coating instead of expensive ALD, which makes the whole synthesis highly cost-effective and easily scalable. Furthermore, we demonstrate the effectiveness of forming heterojunctions to further develop the potential of Cu_2O as a photocathode.

MATERIALS AND METHODS

Sample preparation

The $Cu(OH)_2$ nanowire arrays (NWAs) for heterojunction construction were prepared by anodization of Cu mesh. The Cu mesh (100 mesh, 0.10 mm in wire diameter, Fulun Metal Manufacturing Co., Ltd., Tianjin, China) was sonicated in ethanol and deionized water sequentially for 30 min to remove superficial grease and impurities, followed by anodization in 3 M KOH solution to form $Cu(OH)_2$ NWAs/Cu with Pt counter-electrode at a constant current density of 10 mA cm^{-2} at room temperature until a compliance voltage of 2 V was reached.

To prepare the MO_x/Cu_2O (M = Zn, Ga, Al, Y) heterojunctions, the metal salts (zinc nitrate, 99.9%, and aluminum nitrate, 99.9%, Rhawn, Shanghai, China; gallium nitrate, 99.5%, and yttrium acetate, 99.9%, Energy Chemical, Shanghai, China) were dissolved into ethanolamine (99.5%, Rhawn) and 2-methoxyethanol (99.5%, Rhawn). The obtained solution was added to the $Cu(OH)_2$ NWAs/Cu mesh (geometrical surface area of 3 cm^2) dropwise, followed by annealing in Ar at 600 °C for 4 h. During our initial studies, it is found that the concentration of the precursor solution has a significant impact on the catalytic performance. The concentration used in this work is the best value for each precursor solution: 40, 10, 30 and 40 mM for Zn, Ga, Al and Y, respectively (Table S1 and Fig. S1). To investigate the influence of calcination temperature on the catalytic performance, the Y_2O_3/Cu_2O samples were calcined at 500, 600, and 700 °C for 4 h, respectively.

Structural characterization

The crystalline structure of the samples was analyzed by X-ray diffraction (XRD, Bruker D8 Discover diffractometer, Germany, Cu Kα radiation) over a 2θ range of 20–80° at a scan speed of 5° min^{-1}. The morphologies of the photocathodes were observed by scanning electron microscopy (SEM, Hitachi, Japan, Regulus 8100) and transmission electron microscope (TEM, JEOL, Japan, JEM-F200). The ultraviolet-visible (UV-Vis) diffuse reflectance spectra of the electrodes were recorded using a spectrometer (Perkin Elmer, USA, Lambda 750) equipped with an integrating sphere. X-ray photoelectron spectroscopy (XPS) was conducted on a SPECS system equipped with a XR50 source operating at 150 W and a Phoibos 150 MCD-9 detector. The binding energies were calibrated by C 1s (284.8 eV). Time-resolved photoluminescence (PL) spectroscopy was performed on Fluorolog-3 (HORIBA Jobin Yvon, France) with 532 nm laser. The thermal decomposition of yttrium acetate was characterized using a thermogravimetric analyzer (TGA, Netzsch, Germany, 209F3) at a heating rate of 10 °C min^{-1} in Ar atmosphere.

PEC test

The PEC performance of the electrodes was evaluated in a three-electrode configuration under simulated AM 1.5G illumination on an electrochemical analyzer (CompactStat, Ivium Technologies BV, Netherlands). The electrolyte was a 0.5 M Na_2SO_4 solution buffered at pH 5.0 with potassium phosphate (0.1 M). The reference and counter electrodes were KCl-saturated Ag/AgCl and Pt wire, respectively. The working electrode with exposed area of 0.2 cm^2 was illuminated from the front side. The photo-response was measured under chopped irradiation from a 450 W Xe lamp (SolarEdge700), calibrated with a Si diode to simulate AM 1.5G illumination (100 mW cm^{-2}). The scan rate for linear sweep voltammetry (LSV) and cyclic voltammetry (CV) was 10 mV s^{-1}. Electrochemical impedance spectroscopy (EIS) was performed on Ivium Potentiostat/Galvanostat (Netherlands) with an AC amplitude of 10 mV and frequency range of 10^6–0.1 Hz and DC bias of −0.1 V vs. RHE under AM 1.5G at 25 °C. Photocurrent stability tests were carried out by chronoamperometry, recording the photocurrent produced under chopped light irradiation (light/dark cycles of 4 s) at a fixed electrode potential of 0 V vs. RHE. During LSV and chronoamperometry test, the electrolyte was continuously bubbled with Ar to remove oxygen and eliminate erroneous signals arising from oxygen reduction. Ag/AgCl reference electrode was calibrated before test. All potentials have been referenced to the RHE by the expression: E (vs. RHE) = E (vs. Ag/AgCl) + $E_{Ag/AgCl}$ (vs. SHE) + 0.059×pH.

RESULTS AND DISCUSSION

PEC performance and band alignment of MO_x/Cu_2O heterojunctions

In order to evaluate the PEC performance of the heterostructure, LSV curves were collected. During the LSV scan, the illumination was chopped with a frequency of 0.5 Hz so that the dark and the light currents could be simultaneously monitored.

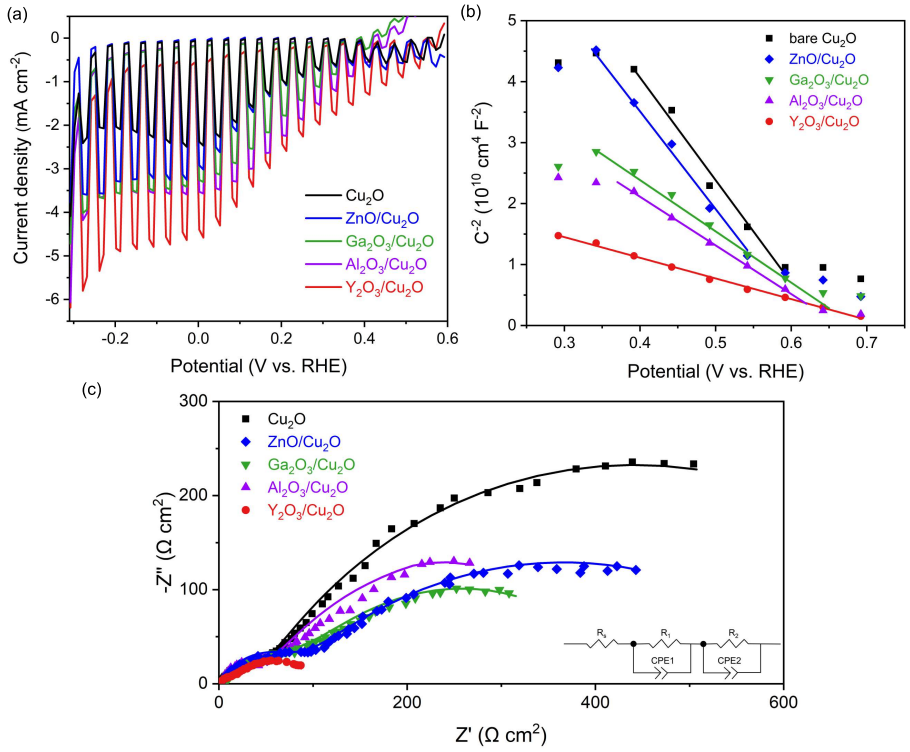

Fig. 1 (a) PEC performance of bare Cu_2O, MO_x/Cu_2O under illumination of chopped AM 1.5G (light on/off cycle: 2 s); (b) Mott-Schottky plot of bare Cu_2O, and MO_x/Cu_2O, measured at 10 kHz; (c) EIS of bare Cu_2O, MO_x/Cu_2O at −0.1 V vs. RHE. The lines are the fitting results with the equivalent circuit inset.

Table 1 Summary of PEC water splitting performance with Cu_2O-based photocathodes under AM 1.5G illumination.

Sample	T (°C)	J (mA cm^{-2})	Flat-band potential (V)	Carrier concentration (cm^{-3})	R_1 (Ω cm^2)	R_2 (Ω cm^2)
bare Cu_2O	600	−2.33	0.64	8.45×10^{18}	57.5	575.7
ZnO/Cu_2O	600	−3.23	0.62	1.01×10^{19}	68.2	388.7
Ga_2O_3/Cu_2O	600	−3.47	0.68	5.06×10^{19}	49.7	303.2
Al_2O_3/Cu_2O	600	−3.56	0.66	7.18×10^{19}	57.3	257.1
Y_2O_3/Cu_2O	600	−4.08	0.72	1.08×10^{20}	25.5	94.8
Y_2O_3/Cu_2O	500	−2.78	0.63	1.35×10^{19}	63.8	387.5
Y_2O_3/Cu_2O	700	−2.56	0.66	1.28×10^{19}	66.4	465.8

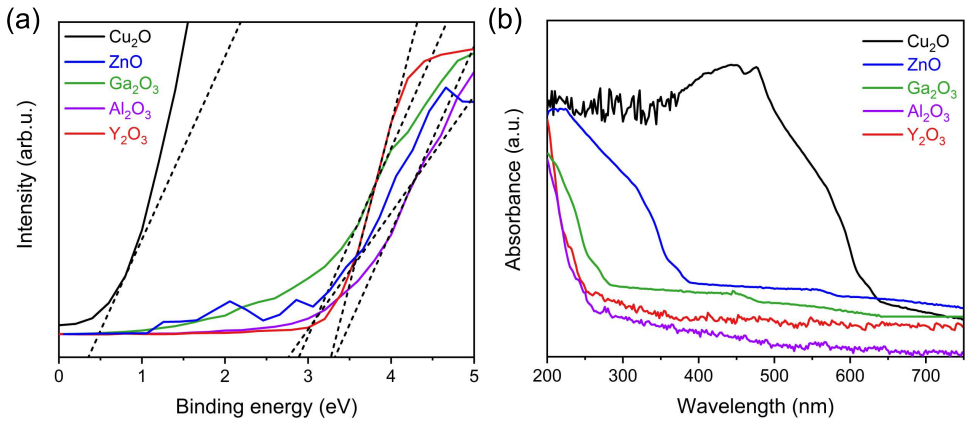

Fig. 2 (a) Valence-band-edge spectra of Cu_2O, ZnO, Ga_2O_3, Al_2O_3, and Y_2O_3; (b) UV-Vis absorption spectra of Cu_2O, ZnO, Ga_2O_3, Al_2O_3, and Y_2O_3.

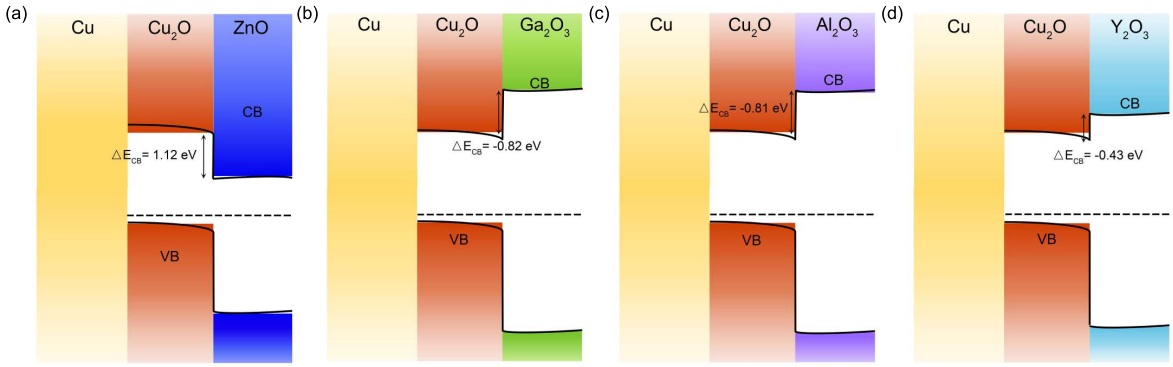

Fig. 3 Equilibrium band-edge diagrams of (a) ZnO/Cu_2O; (b) Ga_2O_3/Cu_2O; (c) Al_2O_3/Cu_2O; and (d) Y_2O_3/Cu_2O heterojunctions.

As shown in Fig. 1a, all the heterojunctions show increased photocurrent compared with the pristine Cu_2O. The corresponding photocurrent at 0 V vs. RHE is −2.33, −3.23, −3.47 and −3.56 mA cm^{-2} for Cu_2O, ZnO/Cu_2O, Ga_2O_3/Cu_2O, and Al_2O_3/Cu_2O, respectively. Y_2O_3/Cu_2O shows the highest photocurrent, −4.08 mA cm^{-2}, which is significantly higher than Ga_2O_3/Cu_2O (−2.95 mA cm^{-2}) [24], ZnS/Cu_2O (−2.3 mA cm^{-2}) [26], TiO_2/Cu_2O (−2.04 mA cm^{-2}) [27], and Al_2O_3/Cu_2O (−1.8 mA cm^{-2}) [28]. It is impressive considering the simple preparation procedure and no deposition of HER electrocatalysts.

Since Mott-Schottky (M-S) analysis can provide information about semiconductor characteristics without damaging its surface, all the samples were subjected to impedance test under dark and the M-S plot is shown in Fig. 1b. All the plots show negative slopes, indicating the p-type conduction behavior. Since the charge carrier density (N_A) is inversely proportional to the slope, all the heterojunctions show smaller slopes than bare Cu_2O; Y_2O_3/Cu_2O shows the lowest slope and thus highest N_A. The resultant flat band potential (V_{FB}) and N_A are listed in Table 1. Comparable Mott-Schottky plots with similar slope patterns were obtained at different measured frequencies (Fig. S2). V_{FB} is 0.62–0.72 V vs. RHE, similar with previous reports [8, 15, 19]. N_A increased for all the heterojunction samples. Among the samples, Y_2O_3/Cu_2O-600 °C showed the highest V_{FB} and N_A, inferring the higher capability of this heterojunction to separate photogenerated electron and hole, leading to increased effective charge carriers. The accumulation of electrons at the Cu_2O-electrolyte interface was reduced, which in turn led to an effective reduction process and ultimately achieved the highest photocurrent density.

EIS was performed in order to understand the charge transfer kinetics of the samples (Fig. 1c). The semicircle at low frequencies is characteristic of the charge transfer process at the electrode/electrolyte interface. The equivalent circuit ($R_c(R_1C_1)(R_2C_2)$) as shown in the inset, where R_s is the solution resistance, while the two RC circuits represent the electron transport within the bulk of the electrode (R_1/C_1) and in the solid electrode/liquid electrolyte interface (R_2/C_2). The good fitting indicates the circuit is reasonable. The fitting results are summarized in Table 1. Y_2O_3/Cu_2O showed the smallest R_1 and R_2, which indicates that the Y_2O_3 layer facilitates the acceptance and transference of the photo-generated electron from Cu_2O to the electrolyte, resulting in a higher PEC activity. Cu_2O displayed a strong fluorescence emission peak centered at ∼630 nm (1.97 eV), corresponding to the exciton luminescence [33]. PL spectra (Fig. S3) reveals that Y_2O_3/Cu_2O sample exhibited the lowest intensity, indicating the lowest recombination rate of photogenerated electron-hole pairs in this sample.

As aforementioned, the energy band alignment is crucial in determining the PEC performance. To investigate the band alignment in detail, we measured the XPS and UV-Vis and the results are shown in Fig. 2. The valence band levels of Cu_2O, ZnO, Ga_2O_3, Al_2O_3, and Y_2O_3 were obtained by linear extrapolation of the valence band edge spectra (Fig. 2a). The core-level binding energy of single metal oxides (Cu_2O, ZnO, Ga_2O_3, Al_2O_3, and Y_2O_3) and heterojunctions (ZnO/Cu_2O, Ga_2O_3/Cu_2O, Al_2O_3/Cu_2O, and Y_2O_3/Cu_2O) were measured by XPS (Fig. S4). The optical band gaps of Cu_2O, ZnO, Ga_2O_3, Al_2O_3, and Y_2O_3 are 2.0, 3.20, 5.20, 5.98, and 5.50 eV, respectively, as derived from the Tauc plots assuming a direct allowed transition (Fig. S5). The band alignment was determined by following the method proposed by Waldrop et al [29] (Table S2) and the results are presented in Fig. 3.

The ZnO/Cu_2O heterojunction shows a large conduction band offset of 1.12 eV, similar with the previous report [30]. Although the conduction band offset is smaller for Ga_2O_3/Cu_2O (−0.82 eV), Al_2O_3/Cu_2O (−0.81 eV), they are still significant. In contrast, Y_2O_3/Cu_2O showed the smallest band offset of −0.43 eV. Since the p-n junction interface is a defect pool, where electron and hole can combine. Reducing the conduction band offset between Cu_2O layer and n-type semiconductor layer can promote the separation

of photo-generated electron and holes, contributing to the high NA and low charge transfer resistance. Accordingly, Y_2O_3 is a better buffer layer for Cu_2O than the well-studied Ga_2O_3 under the present conditions, which is selected for further study.

Crystalline structure and microstructure of Y_2O_3/Cu_2O calcined at different temperatures

Since morphology control is an alternative approach to modify the PEC performance, the Y_2O_3/Cu_2O samples were calcined at different temperatures (500–700 °C). The crystalline structure was first examined by XRD (Fig. 4a). Besides the elemental Cu from the Cu mesh substrate, all the other peaks are attributed to Cu_2O, with strong (111) plane dominating, in consistent with previous reports [8, 10, 31, 32]. The Cu_2O phase was observed as early as 500 °C, indicating the phase transformation from $Cu(OH)_2$ to Cu_2O. No Y_2O_3 was found probably due to its low content and highly-dispersed distribution.

The microstructures of Y_2O_3/Cu_2O samples calcined at different temperatures are shown in Fig. 4b. All the samples maintain the nanowire microstructure with high aspect ratio, which is beneficial for optical absorption along the length and for electron diffusion along the radical direction. However, as the calcination temperature was elevated, the length became shorter and diameter of nanowires became bigger, ∼10 μm and ∼150 nm, respectively, at 500 °C. When the temperature was increased to 700 °C, the NWAs started to collapse and form necklace. To demonstrate the formation of Y_2O_3 on Cu_2O NWAs, TEM was run on 600 °C-calcined sample and the result is shown in Fig. 4c. The Cu_2O NAWs had an average diameter of ∼200 nm discretely decorated with Y_2O_3 particles. The lattice fringe spacing of 0.246 and 0.167 nm matches well with the (111) crystal plane of Cu_2O and the (026) crystal plane of Y_2O_3, respectively. The elemental mapping result reveals the rather homogeneous distribution of Y_2O_3 on the surface of Cu_2O nanowires, with size below the detection limit of XRD (Fig. 4a).

PEC performance of Y_2O_3/Cu_2O calcined at different temperatures

Based on the microstructure evolution, the samples calcined at different temperatures probably show different PEC catalytic performance. To explore that, LSV was measured and the results are shown in Fig. 5a. The calcination temperature had an obvious effect on the PEC activity. All the calcined Y_2O_3/Cu_2O showed higher photocurrent density than the bare Cu_2O (600 °C-calcined). The activity increased remarkably when the calcination temperature was increased from 500 (−2.78 mA cm^{-2} at 0 V vs. RHE) to 600 °C (−4.08 mA cm^{-2}), but decreased quickly when the temperature was further increased to 700 °C (−2.56 mA cm^{-2}), even lower than that of 500 °C-samples, probably due to reduced surface area induced by sintering. The lower activity of 500 °C samples is probably because yttrium acetate is not completely converted to Y_2O_3 when annealed at 500 °C and $Y_2(CO_3)_3$ remains based on the TGA result. The Y_2O_3/Cu_2O heterojunction structure cannot be formed, resulting in low photocurrent density.

Based on the EIS results (Fig. 5b), the decoration with Y_2O_3 significantly facilitates the charge-transfer process, as evidenced by the obviously reduced R_2 arc. Especially, Y_2O_3/Cu_2O calcined at 600 °C showed the lowest R_2, which contributes to the high PEC activity. The V_{FB} and N_A values of all the samples derived from the M-S plot (Fig. 5c) are listed in Table 1. Among the samples, the 600 °C calcined sample showed the highest V_{FB} and N_A, which contributes to the high PEC activity.

To further explore the charge carrier recombination properties of those samples, PL spectroscopy was run and the results are shown in Fig. 5d. The Y_2O_3 modification reduced the PL intensity substantially. Y_2O_3/Cu_2O-600 °C showed the lowest intensity, a strong indicator of the lowest recombination rate of photogenerated electron-hole pairs in this sample, which is beneficial for PEC activity.

Since the photo-stability is a great concern for Cu_2O-based photocathode, the effect of Y_2O_3 coating on the photo-stability was examined with chronoamperometric measurement over 10 min. The bare Cu_2O NWAs photocathode degraded quickly, with only 20.4% of initial current density after 600 s (Fig. 6a). In sharp contrast, the photo-stability was remarkably increased for Y_2O_3/Cu_2O, with retention of 68.1%. Since the coating of Y_2O_3 on Cu_2O was not conformal as ALD, the protection effect was limited; the photocorrosion triggered by the contact of Cu_2O with aqueous solution was inevitable. The postmortem analysis (Fig. S6) reveals that the nanowire heterojunction was well maintained; however, CuO was found due to the photocorrosion during test, which should be mainly responsible for the stability degradation.

The performance is comparable with the reported carbon coated Cu_2O nanowires (61.3% after 10 min irradiation) [34], NiO coated Cu_2O (72% after 20 min irradiation) [32], TiO_2 coated Cu_2O (33% after 20 min irradiation) [11], ZnO/TiO_2 coated Cu_2O (51.6% after 10 min irradiation) [35], and g-C_3N_4 coated Cu_2O (55% after 20 min irradiation) [23]. Although the Y_2O_3/Cu_2O junction can alleviate the charge accumulation at the interface between Cu_2O and Y_2O_3, the sharp rise and fall of the photocurrent in Fig. 6a is due to the charge accumulation at the Cu_2O/electrolyte interface, which needs to be addressed in the future.

Finally, the photoconversion efficiency (η) of the photocathode is calculated from its current-voltage data [36]. As shown in Fig. 6b, the maximum η for the bare Cu_2O NWAs is 0.22%, while the Y_2O_3/Cu_2O NWAs attains a much higher maximum photoconversion efficiency of 0.59% at the potential of 0.3 V vs.

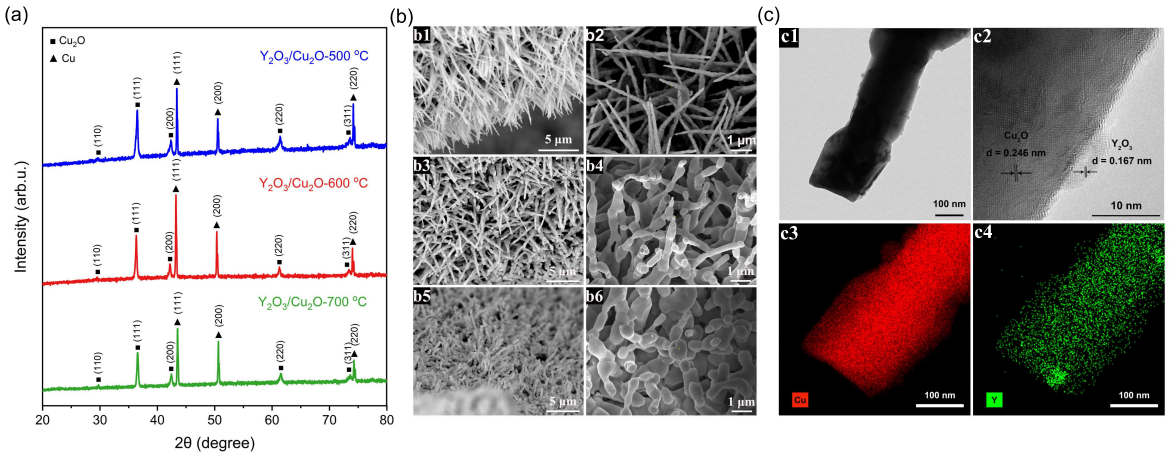

Fig. 4 (a) XRD patterns of Y_2O_3/Cu_2O-500, 600, 700 °C NWAs; (b) SEM images of Y_2O_3/Cu_2O NWAs calcined at 500 °C (b1, b2), 600 °C (b3, b4) and 700 °C NWAs (b5, b6); (c) TEM and HRTEM images of Y_2O_3/Cu_2O-600 °C NWAs (c1, c2), element mapping of Cu and Y (c3, c4).

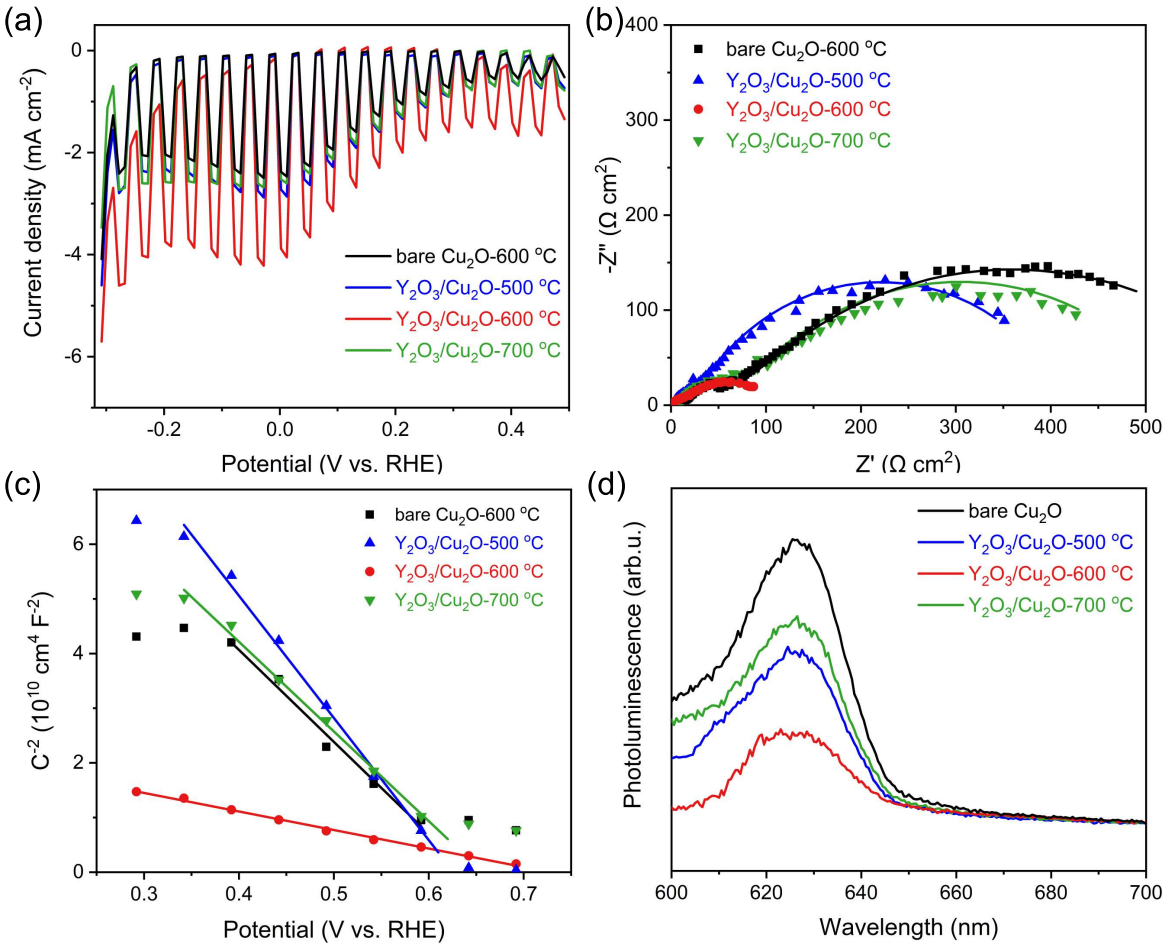

Fig. 5 (a) PEC performance; (b) EIS at −0.1 V vs. RHE; (c) M-S plot; (d) PL spectra of the bare Cu_2O, Y_2O_3/Cu_2O-500, 600, 700 °C NWAs.

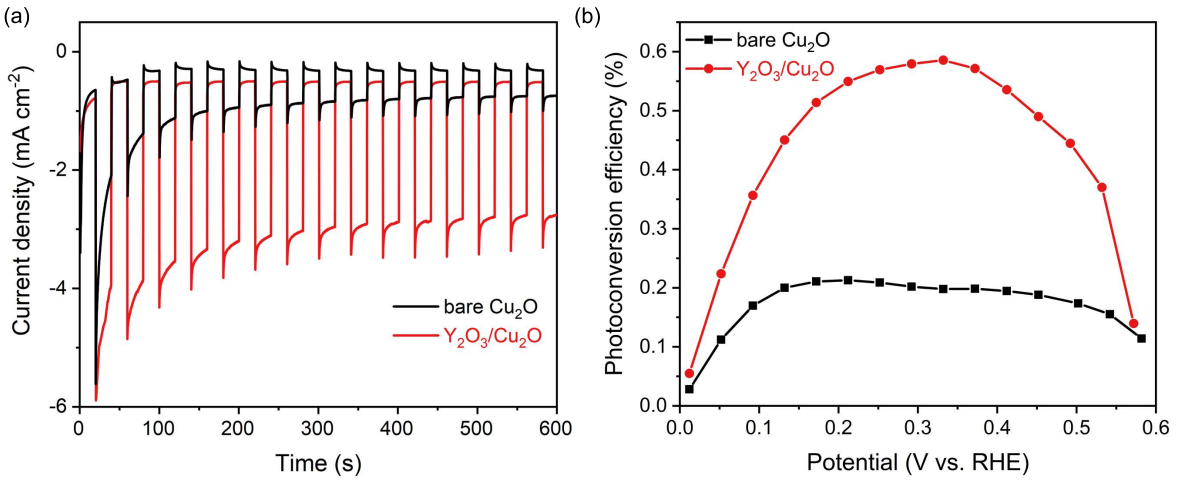

Fig. 6 (a) PEC stability tests of Cu_2O and Y_2O_3/Cu_2O NWAs at a biased potential of 0 V vs. RHE; (b) The plot of photoconversion efficiencies vs applied bias potentials for Cu_2O and Y_2O_3/Cu_2O NWAs.

RHE. The performance is comparable with the reported p-Cu_2O/n-Cu_2O (0.50% at 0.35 V vs. RHE) [37], and C/Cu_2O (0.56% at 0.21 V vs. RHE) [38]. This work provides a simple method for solution-based modification of Cu_2O photocathodes, which should be enlightening for practical PEC water splitting.

CONCLUSION

We demonstrate that Y_2O_3 is a promising buffer layer for p-type Cu_2O for PEC water splitting considering its cost-effectiveness and facile preparation. The underlying reason is better band alignment with Cu_2O, which effectively alleviate the recombination of charge-carriers at the interface of heterojunction. Tuning the band alignment is proved an effective strategy to improve the PEC performance of Cu_2O. The Y_2O_3/Cu_2O heterojunction calcined at 600 °C showed higher PEC activity with photocurrent of −4.08 mA cm^{-2} at 0 V vs. RHE under AM 1.5G illumination, better stability with 68.1% over 10 min duration, and higher photoconversion efficiency of 0.59% at 0.3 V vs. RHE.

Appendix A. Supplementary data

Supplementary data associated with this article can be found at https://dx.doi.org/10.2306/scienceasia1513-1874.2026.048.

Acknowledgements: This work was funded by the National Natural Science Foundation of China (Grant No. 51702230).

REFERENCES

1. Hisatomi T, Kubota J, Domen K (2014) Recent advances in semiconductors for photocatalytic and photoelectrochemical water splitting. *Chem Soc Rev* **43**, 7520–7535.
2. Fujishima A, Honda K (1972) Electrochemical photolysis of water at a semiconductor electrode. *Nature* **238**, 37–38.
3. Guo Q, Zhou C, Ma Z, Yang X (2019) Fundamentals of TiO_2 photocatalysis: concepts, mechanisms, and challenges. *Adv Mater* **31**, 1901997.
4. Sharma P, Jang JW, Lee JS (2019) Key Strategies to advance the photoelectrochemical water splitting performance of alpha-Fe_2O_3 photoanode. *ChemCatChem* **11**, 157–179.
5. Kim JH, Lee JS (2019) Elaborately modified $BiVO_4$ photoanodes for solar water splitting. *Adv Mater* **31**, 1806938.
6. Bagal IV, Chodankar NR, Hassan MA, Waseem A, Johar MA, Kim DH, Ryu SW (2019) Cu_2O as an emerging photocathode for solar water splitting: A status review. *Int J Hydrogen Energy* **44**, 21351–21378.
7. Li C, He J, Xiao Y, Li Y, Delaunay JJ (2020) Earth-abundant Cu-based metal oxide photocathodes for photoelectrochemical water splitting. *Energy Environ Sci* **13**, 3269–3306.
8. Luo J, Steier L, Son MK, Schreier M, Mayer MT, Grätzel M (2016) Cu_2O nanowire photocathodes for efficient and durable solar water splitting. *Nano Lett* **16**, 1848–1857.
9. Kurniawan M, Stich M, Marimon M, Camargo M, Peipmann R, Hannappel T, Bund A (2021) Electrodeposition of cuprous oxide on a porous copper framework for an improved photoelectrochemical performance. *J Mater Sci* **56**, 11866–11880.
10. Hacialioglu S, Meng F, Jin S (2012) Facile and mild solution synthesis of Cu_2O nanowires and nanotubes driven by screw dislocations. *Chem Commun* **48**, 1174–1176.
11. Paracchino A, Laporte V, Sivula K, Grätzel M, Thimsen E (2011) Highly active oxide photocathode for photoelectrochemical water reduction. *Nat Mater* **10**, 456–461.
12. Pan L, Kim JH, Mayer MT, Son MK, Ummadisingu A, Lee JS, Hagfeldt A, Luo J, et al (2018) Boosting the performance of Cu_2O photocathodes for unassisted solar water splitting devices. *Nat Catal* **1**, 412–420.
13. Li C, Hisatomi T, Watanabe O, Nakabayashi M, Shibata N, Domen K, Delaunay JJ (2016) Simultaneous enhancement of photovoltage and charge transfer in Cu_2O-based photocathode using buffer and protective layers. *Appl*

Phys Lett **109**, 3902.
14. Dasgupta NP, Liu C, Andrews S, Prinz FB, Yang P (2013) Atomic layer deposition of platinum catalysts on nanowire surfaces for photoelectrochemical water reduction. *J Am Chem Soc* **135**, 12932–12935.
15. Niu W, Zhu L, Wang Y, Lou Z, Ye Z (2017) Interfacial study of $Cu_2O/Ga_2O_3/AZO/TiO_2$ photocathode for water splitting fabricated by pulsed laser deposition. *Catal Sci Technol* **7**, 1602–1610.
16. Nantaouppakan W, Comsup N (2025) Effects of calcination heating rate on the photocatalytic activity of Al-doped TiO_2 nanofibers. *ScienceAsia* **51**, 2026001.
17. Minami T, Nishi Y, Miyata T (2013) High-efficiency Cu_2O-based heterojunction solar cells fabricated using a Ga_2O_3 thin film as n-type layer. *Appl Phys Express* **6**, 044101.
18. Li W, Wang H, Sun Z, Wu Q, Xue S (2021) Si-doped Cu_2O/SiO_x composites for efficient photoelectrochemical water reduction. *J Power Sources* **492**, 229667.
19. Ma X, Zhang J, Wang B, Li Q, Chu S (2018) Hierarchical Cu_2O foam/g-C_3N_4 photocathode for photoelectrochemical hydrogen production. *Appl Surf Sci* **427**, 907–916.
20. Tawfik WZ, Hassan MA, Johar MA, Ryu SW, Lee JK (2019) Highly conversion efficiency of solar water splitting over p-Cu_2O/ZnO photocatalyst grown on a metallic substrate. *J Catal* **374**, 276–283.
21. Azevedo J, Tilley SD, Schreier M, Stefik M, Sousa C, Araújo JP, Mendes A, Grätzel M, et al (2016) Tin oxide as stable protective layer for composite cuprous oxide water-splitting photocathodes. *Nano Energy* **24**, 10–16.
22. Xu X, Liu Y, Zhu Y, Fan X, Li Y, Zhang F, Zhang G, Peng W (2017) Fabrication of a Cu_2O/g-C_3N_4/WS_2 triple-layer photocathode for photoelectrochemical hydrogen evolution. *ChemElectroChem* **4**, 1498–1502.
23. Zhang S, Yan J, Yang S, Xu Y, Cai X, Li X, Zhang X, Peng F, et al (2017) Electrodeposition of Cu_2O/g-C_3N_4 heterojunction film on an FTO substrate for enhancing visible light photoelectrochemical water splitting. *J Catal* **38**, 365–371.
24. Li C, Hisatomi T, Watanabe O, Nakabayashi M, Shibata N, Domen K, Delaunay JJ (2015) Positive onset potential and stability of Cu_2O-based photocathodes in water splitting by atomic layer deposition of a Ga_2O_3 buffer layer. *Energy Environ Sci* **8**, 1493–1500.
25. Niu W, Moehl T, Cui W, Wick-Joliat R, Zhu L, Tilley SD (2018) Extended light harvesting with dual Cu_2O-based photocathodes for high efficiency water splitting. *Adv Energy Mater* **8**, 1702323.
26. Dai P, Li W, Xie J, He Y, Thorne J, McMahon G, Zhan J, Wang D (2014) Forming buried junctions to enhance the photovoltage generated by cuprous oxide in aqueous solutions. *Angew Chem Int Ed* **126**, 13711–13715.
27. Choi J, Song JT, Jang HS, Choi MJ, Sim DM, Yim S, Lim H, Jung YS, et al (2017) Interfacial band-edge engineered TiO_2 protection layer on Cu_2O photocathodes for efficient water reduction reaction. *Mater Lett* **13**, 57–65.
28. Ho-Kimura S, Moniz SJA, Tang J, Parkin IPA (2015) Method for synthesis of renewable Cu_2O junction composite electrodes and their photoelectrochemical properties. *ACS Sustain Chem Eng* **3**, 710–717.
29. Waldrop JR, Grant RW, Kowalczyk SP, Kraut EA (1985) Measurement of semiconductor heterojunction band discontinuities by X-ray photoemission spectroscopy. *J Vac Sci Technol A* **3**, 835–841.
30. Yang M, Zhu L, Li Y, Cao L, Guo Y (2013) Asymmetric interface band alignments of Cu_2O/ZnO and ZnO/Cu_2O heterojunctions. *J Alloy Compd* **578**, 143–147.
31. Paracchino A, Brauer JC, Moser JE, Thimsen E, Grätzel M (2012) Synthesis and characterization of high-photoactivity electrodeposited Cu_2O solar absorber by photoelectrochemistry and ultrafast spectroscopy. *J Phys Chem C* **116**, 7341–7350.
32. Lin CY, Lai YH, Mersch D, Reisner E (2012) Cu_2O vertical bar NiO_x nanocomposite as an inexpensive photocathode in photoelectrochemical water splitting. *Chem Sci* **3**, 3482–3487.
33. Ito T, Masumi T (1997) Detailed examination of relaxation processes of excitons in photoluminescence spectra of Cu_2O. *J Phys Soc Jpn* **66**, 2185–2193.
34. Shi W, Zhang X, Li S, Zhang B, Wang M, Shen Y (2015) Carbon coated Cu_2O nanowires for photoelectrochemical water splitting with enhanced activity. *Appl Surf Sci* **358**, 404–411.
35. Kargar A, Partokia SS, Niu MT, Allameh P, Yang M, May S, Cheung JS, Sun K, et al (2014) Solution-grown 3D Cu_2O networks for efficient solar water splitting. *Nanotechnology* **25**, 205401.
36. Walter MG, Warren EL, McKone JR, Boettcher SW, Mi Q, Santori EA, Lewis NS (2010) Solar water splitting cells. *Chem Rev* **110**, 6446–6473.
37. Wang T, Wei Y, Chang X, Li C, Li A, Liu S, Zhang J, Gong J (2018) Homogeneous Cu_2O p-n junction photocathodes for solar water splitting. *Appl Catal B Environ* **226**, 31–37.
38. Zhang Z, Dua R, Zhang L, Zhu H, Zhang H, Wang P (2013) Carbon-layer-protected cuprous oxide nanowire arrays for efficient water reduction. *ACS Nano* **7**, 1709–1717.

Appendix A. Supplementary data

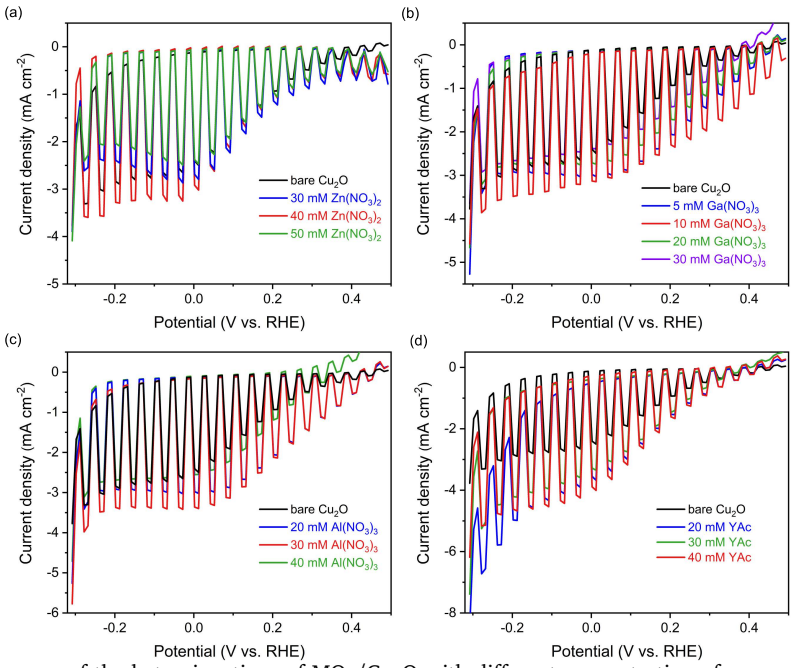

Fig. S1 PEC performance of the heterojunctions of MO_x/Cu_2O with different concentration of precursors. (a) ZnO/Cu_2O; (b) Ga_2O_3/Cu_2O; (c) Al_2O_3/Cu_2O; (d) Y_2O_3/Cu_2O.

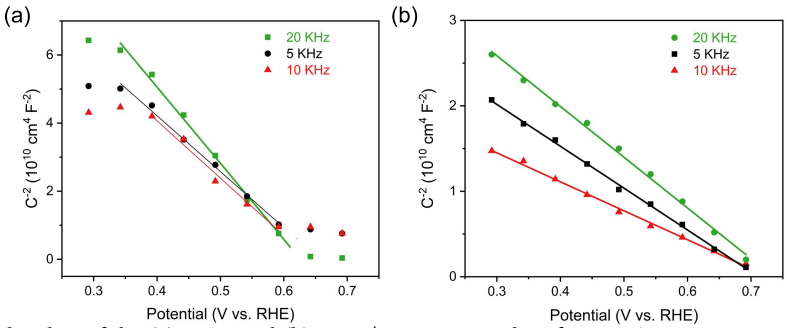

Fig. S2 Mott–Schottky plots of the (a) Cu_2O and (b) Y_2O_3/Cu_2O at 5–20 kHz frequencies.

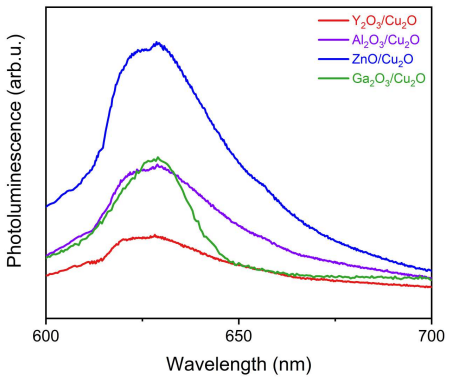

Fig. S3 PL spectra of Ga_2O_3/Cu_2O, ZnO/Cu_2O, Al_2O_3/Cu_2O, and Y_2O_3/Cu_2O.

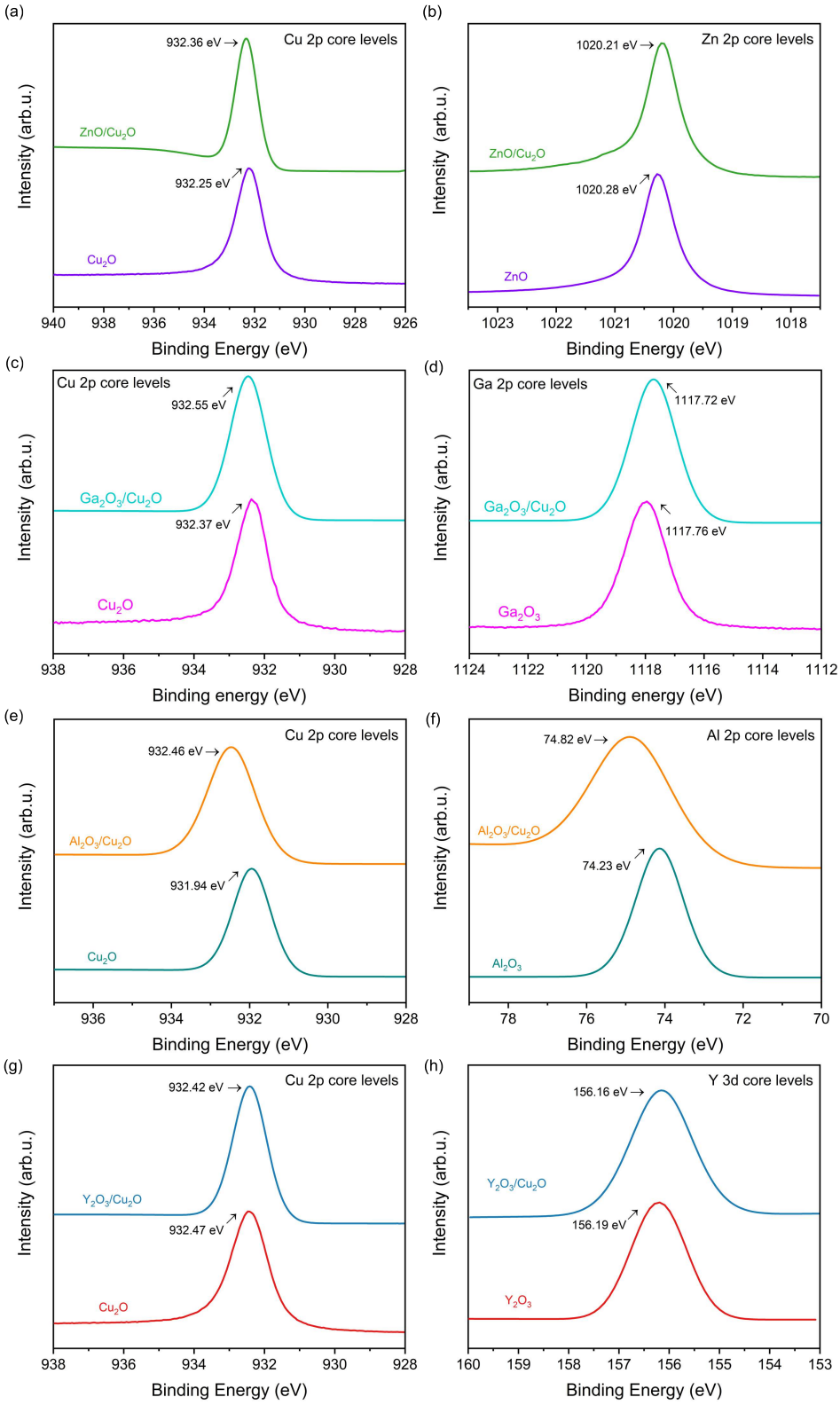

Fig. S4 XPS measurements. (a) Cu 2p core levels of bulk Cu_2O and ZnO/Cu_2O; (b) Zn 2p core levels of bulk ZnO and ZnO/Cu_2O; (c) Cu 2p core levels of bulk Cu_2O and Ga_2O_3/Cu_2O; (d) Ga 2p core levels of bulk Ga_2O_3 and Ga_2O_3/Cu_2O; (e) Cu 2p core levels of bulk Cu_2O and Al_2O_3/Cu_2O; (f) Al 2p core levels of bulk Al_2O_3 and Al_2O_3/Cu_2O; (g) Cu 2p core levels of bulk Cu_2O and Y_2O_3/Cu_2O; (h) Y 3d core levels of bulk Y_2O_3 and Y_2O_3/Cu_2O.

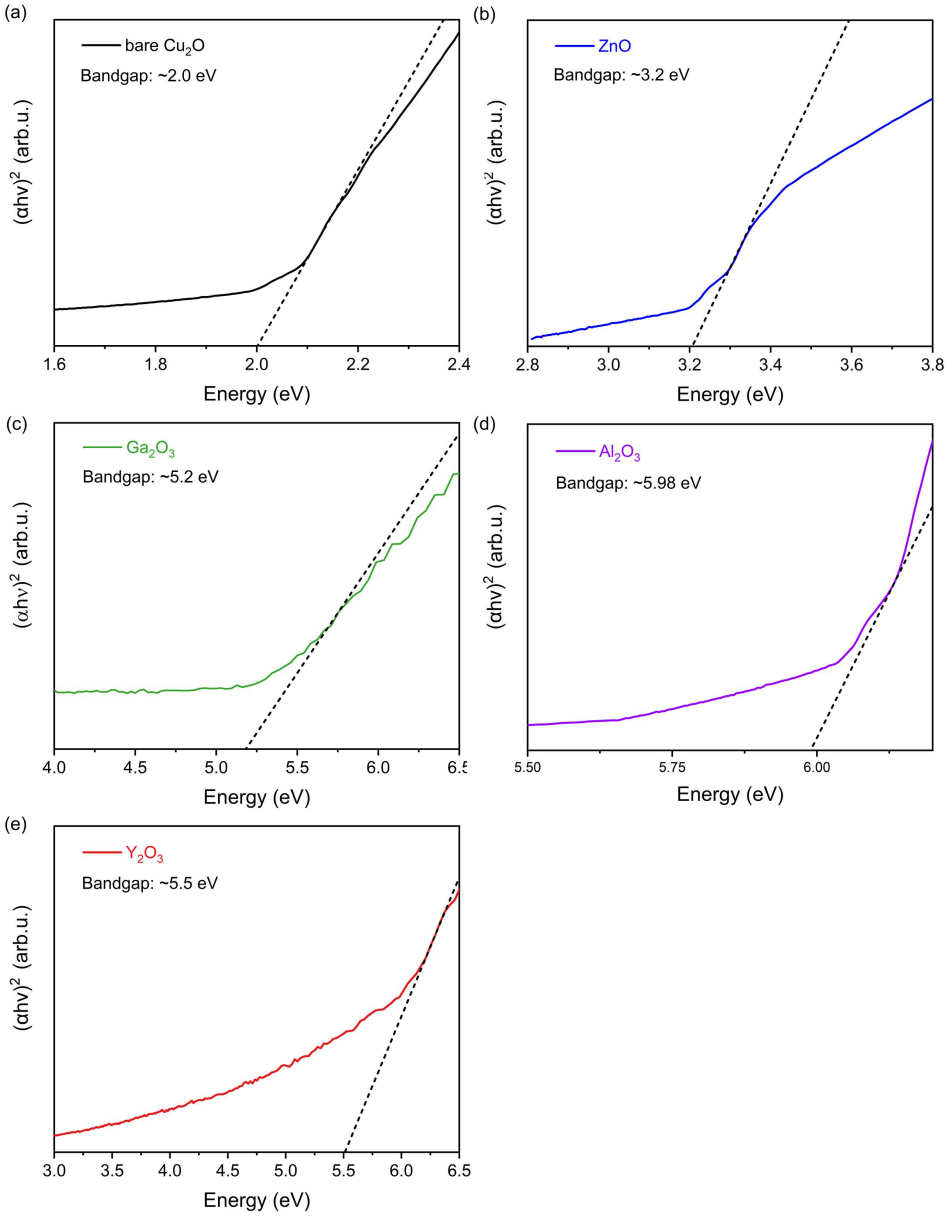

Fig. S5 Tauc plots of (a) Cu_2O; (b) ZnO; (c) Ga_2O_3; (d) Al_2O_3; and (e) Y_2O_3.

Table S1 Summary of photocathodes current density prepared from different concentrations of Zn, Ga, Al, and Y precursor solutions.

Sample	J (mA cm^{-2})	Sample	J (mA cm^{-2})	Sample	J (mA cm^{-2})	Sample	J (mA cm^{-2})
	-	5 mM Ga	−2.69	-	-	-	-
	-	10 mM Ga	−3.47	-	-	-	-
30 mM Zn	−2.69	20 mM Ga	−3.25	20 mM Al	−3.24	20 mM Y	−3.52
40 mM Zn	−3.26	30 mM Ga	−3.03	30 mM Al	−3.58	30 mM Y	−3.75
50 mM Zn	−2.42	40 mM Ga	−3.08	40 mM Al	−2.55	40 mM Y	−4.08

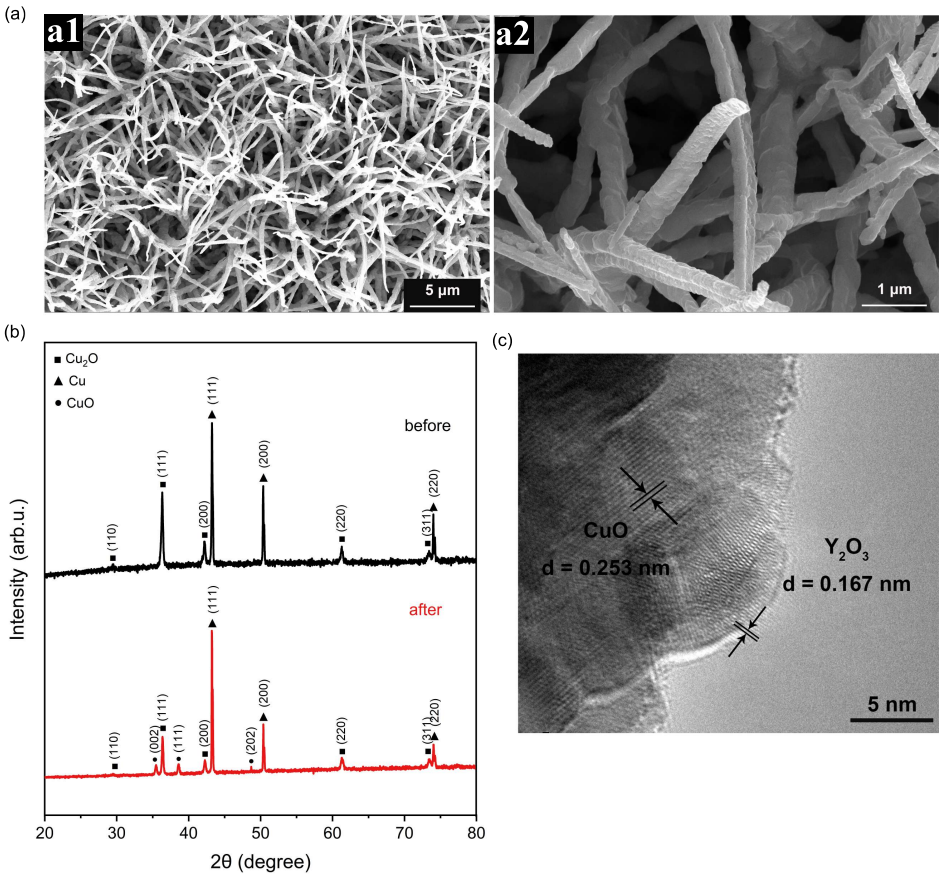

Fig. S6 SEM, XRD, and TEM image of Y_2O_3/Cu_2O that has undergone the PEC stability test.

Table S2 Test results used to determine values of ZnO/Cu_2O, Ga_2O_3/Cu_2O, Al_2O_3/Cu_2O, and Y_2O_3/Cu_2O band offset.

Sample	Core Cu 2p (eV)	Core Y 3d (eV)	Ev (eV)	Ec (eV)
Cu_2O	932.25	-	0.30	-
ZnO	-	1020.28	2.80	-
ZnO/Cu_2O	932.36	1020.21	-	1.12
Cu_2O	932.37	-	0.30	-
Ga_2O_3	-	1117.76	2.90	-
Ga_2O_3/Cu_2O	932.55	1117.72	-	−0.82
Cu_2O	931.94	-	0.30	-
Al_2O_3	-	74.23	3.4	-
Al_2O_3/Cu_2O	932.46	74.82	-	−0.81
Cu_2O	932.47	-	0.30	-
Y_2O_3	-	156.19	3.35	-
Y_2O_3/Cu_2O	932.42	156.16	-	−0.43